

Differential Activity-Driven Instabilities in Biphasic Active Matter

Christoph A. Weber,¹ Chris H. Rycroft,^{1,2} and L. Mahadevan^{3,*}

¹*Paulson School of Engineering and Applied Sciences, Harvard University, Cambridge, Massachusetts 02138, USA*

²*Mathematics Group, Lawrence Berkeley National Laboratory, Berkeley, California 94720, USA*

³*Paulson School of Engineering and Applied Sciences, Department of Physics, Department of Organismic and Evolutionary Biology, Harvard University, Cambridge, Massachusetts 02138, USA*



(Received 9 October 2017; revised manuscript received 25 February 2018; published 12 June 2018)

Active stresses can cause instabilities in contractile gels and living tissues. Here we provide a generic hydrodynamic theory that treats these systems as a mixture of two phases of varying activity and different mechanical properties. We find that differential activity between the phases causes a uniform mixture to undergo a demixing instability. We follow the nonlinear evolution of the instability and characterize a phase diagram of the resulting patterns. Our study complements other instability mechanisms in mixtures driven by differential adhesion, differential diffusion, differential growth, and differential motion.

DOI: [10.1103/PhysRevLett.120.248003](https://doi.org/10.1103/PhysRevLett.120.248003)

Biological systems are distinguished by the presence of active stresses that affect their properties and alter their stability. For example, active stresses give rise to collectively moving streaks [1] and clusters [2–4], rotating ring, swirl or asterlike patterns [5–10], or the remodeling of cell-to-cell junctions in living tissues [11]. These systems are typically described as a single phase with active stresses that drive the assembly of the constituents, and the properties of the phases are typically assumed to be similar to liquids [12–14] or even gases [15–18].

However, many active materials cannot be treated as fluids. Examples include cartilage, bone, tissues in early development, and superprecipitated systems, such as networks of filaments connected by cross-links and molecular motors. The presence of activity in these systems drives the macroscopic contraction of gels [9,10,19], the compaction of cells during the condensation of cartilage [20], the formation of osteoblast networks [21], and the formation of furrows and tubes in tissues [22,23], and even cytoplasmic contractility in cells [24,25]. All these systems are composed of multiple phases with different rheological properties and are subject to multiple types of active forcing. This differential activity can cause instabilities in a variety of systems, such as chromosome positioning [26], and demixing in polydisperse and polythermal colloidal mixtures [27,28,29]. Thus, we need to go beyond one-component descriptions used to describe isotropic active gels [12,23–25] and include a more general biphasic description [30,31]. While recent work has included activity in a poroelastic description [32,33], the material was assumed to be homogeneous and stable despite active stress generation in one of the phases. Here we relax this assumption of the stability of an active mixture composed of two phases with different activity and different mechanical properties, and determine the physical conditions under which an

active poroelastic material might contract (condense) or disintegrate (fragment).

We start with a consideration of isotropic active systems composed of two immiscible phases, $i = 1, 2$. These systems can be described by a hydrodynamic theory similar to descriptions used for fluidlike biphasic matter [34,35] or elastic [36] and viscoelastic gels [37,38]. This theory is valid on length scales above the characteristic pore size of the solidlike phase. At the simplest level, activity in our biphasic system is described as an isotropic active stress that acts on each phase that responds to this stress according to its passive mechanical properties, which are either fluid or solidlike, respectively. Each phase (i) is described by the hydrodynamic variables: velocity $v_\alpha^{(i)}$, volume fraction $\phi^{(i)}$, and displacement $u_\alpha^{(i)}$ with $\partial_t u_\alpha^{(i)} = v_\alpha^{(i)}$. The overall system is assumed to be incompressible and fully occupied by the two phases, i.e., $\phi \equiv \phi^{(1)} = 1 - \phi^{(2)}$. The fractions of each phase i are conserved, so that $\partial_t \phi^{(i)} = -\partial_\alpha (\phi^{(i)} v_\alpha^{(i)} + j_\alpha^{(i)})$, where $j_\alpha^{(i)}$ denotes a relative flux between the phases with $j_\alpha^{(1)} = -j_\alpha^{(2)} \equiv j_\alpha$. This relative flux can, for example, stem from rare unbinding events of components that belong to one of the phases. The resulting unbound components can diffuse and thereby cause an effective diffusive flux of the bound components (see Supplemental Material [39], Sec. I). For simplicity, we write $j_\alpha = -D \partial_\alpha \phi$, where D denotes the diffusion constant. The two mass conservation laws can then be equivalently expressed by one transport equation and an incompressibility condition,

$$\partial_t \phi = -\partial_\alpha (\phi v_\alpha^{(1)}) + D \partial_\alpha^2 \phi, \quad (1a)$$

$$0 = \partial_\alpha [\phi v_\alpha^{(1)} + (1 - \phi) v_\alpha^{(2)}]. \quad (1b)$$

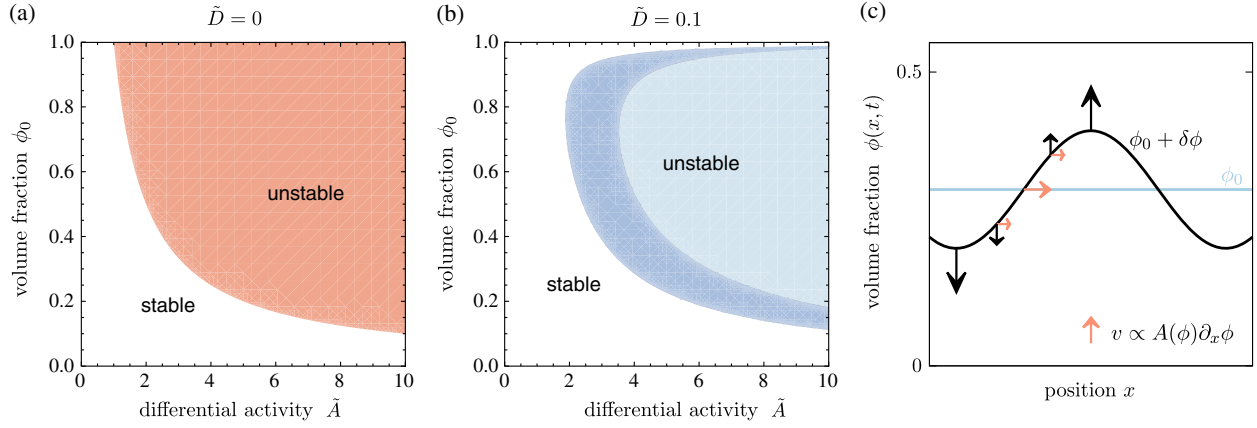


FIG. 1. (a),(b) Stability diagrams as a function of volume fraction ϕ and nondimensional constant differential activity \tilde{A} obtained from the linear stability analysis of Eqs. (3), for different choices of diffusivity (a) $\tilde{D} = 0$ and (b) $\tilde{D} = 0.1$. The colored regions depict $\Re(\omega_+) > 0$. Red indicates an instability where $\Im(\omega_k) = 0$, corresponding to exponential growth, while dark (light) blue corresponds to $\Im(\omega_k) \neq 0$ for all wave numbers (for a finite band of wave numbers). (c) Illustration of the instability mechanism driven by differential activity $A(\phi)$. Small perturbations in volume fraction $\phi_0 \rightarrow \phi_0 + \delta\phi$ are amplified since differential activity causes a drift velocity $v = \dot{u}$ that points toward the maximum of a local inhomogeneity of volume fraction. To lowest order in q , this velocity (red horizontal arrows) scales as $v \propto A(\phi)\partial_x\phi$ [Eq. (5)], further increasing the initial perturbation as indicated by vertical black lines.

Neglecting osmotic effects and inertia, force balance in each phase implies

$$0 = \partial_\beta(\phi\sigma_{\alpha\beta}^{(1)}) - \phi\partial_\alpha p - \mathcal{F}_\alpha, \quad (2a)$$

$$0 = \partial_\beta((1-\phi)\sigma_{\alpha\beta}^{(2)}) - (1-\phi)\partial_\alpha p + \mathcal{F}_\alpha, \quad (2b)$$

where $\sigma_{\alpha\beta}^{(i)}$ is the additional stress (beyond the pressure) in each phase, and we have assumed, as in mixture theory [44–46], that this stress is weighted by the respective volume fraction [47]. The pressure p acts as a Lagrange multiplier that ensures the incompressibility condition (1). Momentum transfer between the phases is described by a friction force density \mathcal{F} . To leading order \mathcal{F} is proportional to the relative velocity of the phases, $\mathcal{F}_\alpha = \Gamma(\phi)(v_\alpha^{(1)} - v_\alpha^{(2)})$, where $\Gamma(\phi) = \Gamma_0\phi(1-\phi)$ is the friction coefficient between the phases with Γ_0 constant. The dependence of the friction coefficient on volume fraction is a consequence of the condition that hydrodynamic momentum transfer vanishes if one of the phases is absent, i.e., $\mathcal{F} = 0$ for $\phi = 0$ or $\phi = 1$. Finally, we additively decompose the stress into the passive stress $\sigma_{\alpha\beta}^{(i),p}$ and the isotropic activity $A^{(i)}$,

$$\sigma_{\alpha\beta}^{(i)} = \sigma_{\alpha\beta}^{(i),p} + A^{(i)}\delta_{\alpha\beta}, \quad (2c)$$

where the passive stress $\sigma_{\alpha\beta}^{(i),p}$ characterizes the mechanical properties of each phase. In general, the activity depends on all hydrodynamic variables. For simplicity, we focus on activities that depend on the volume fraction ϕ , $A^{(i)} = A^{(i)}(\phi)$. Eqs. (2) can be rewritten as

$$0 = \partial_\beta(\phi\sigma_{\alpha\beta}^{(1)} + (1-\phi)\sigma_{\alpha\beta}^{(2)} - \delta_{\alpha\beta}p), \quad (3a)$$

$$0 = \partial_\beta(\phi\sigma_{\alpha\beta}^{(1),p}) - \frac{\phi}{1-\phi}\partial_\beta((1-\phi)\sigma_{\alpha\beta}^{(2),p}) + (v_\alpha^{(2)} - v_\alpha^{(1)})\Gamma_0\phi + \phi A(\phi)\partial_\alpha\phi, \quad (3b)$$

where we define

$$A(\phi) = \left(\frac{A^{(1)}}{\phi} + \frac{A^{(2)}}{1-\phi} + \frac{d}{d\phi}(A^{(1)} - A^{(2)}) \right) \quad (3c)$$

as the “differential activity.” The derivatives of the activity $A^{(i)}$ with respect to ϕ appear because gradients of stress enter the force balance Eqs. (2a) and (2b), while the dependencies on the activity $A^{(i)}$ are a consequence of treating the system as a biphasic mixture, i.e., weighting the stress contributions by the respective volume fractions; see Supplemental Material [39], Sec. III for more details on Eq. (3c). The specific form of the activities $A^{(i)}$ depends on the system of interest.

To complete our description, we have to select constitutive equations for the passive stress of each phase. Depending on the type of multiphase system, such as physical or chemical gels, tissue mixtures or mixtures composed of active colloids, we may consider solid, fluid, or viscoelastic stress-strain or stress-strain-rate relationships. However, to illustrate the generic but multiphase specific dynamic properties, we restrict ourselves to a simple example of a one-dimensional, biphasic mixture composed of a (Kelvin) viscoelastic solid (s) and a fluid phase (f), with the constitutive equations

$$\sigma^{s,p} = \lambda \partial_x u + \zeta \partial_x v, \quad (4a)$$

$$\sigma^{f,p} = 0, \quad (4b)$$

where the one-dimensional solid displacement and velocity are u and $v = du/dt \equiv \dot{u}$; the fluid velocity is given by $-v\phi/(1-\phi)$. In Eq. (4a), λ denotes the Lamé coefficient and ζ is the bulk solid viscosity. The viscous stress in the fluid phase can be approximated to zero since fluid strains are negligible relative to solid strains on length scales above the pore size, and in the systems of interest, the solid viscosity typically exceeds the fluid viscosity by several orders in magnitude [48]. Moreover, an additional fluid viscosity does not affect the occurrence of an instability. Since diffusive transport of constituents in this solid-fluid mixture is expected to be slow compared to solid momentum transport, we consider the limit of small diffusivities and use rescalings of length and timescales not containing the diffusion constant. Specifically, we rescale time and length as $t \rightarrow (\zeta/\lambda)t$ and $x \rightarrow \ell x$ with $\ell = \sqrt{\zeta/\Gamma_0}$, so that velocities $v \rightarrow v\ell\lambda/\zeta$ and the scaled equations read

$$\partial_t \phi = -\partial_x(\phi \dot{u}) + \tilde{D} \partial_x^2 \phi, \quad (5a)$$

$$0 = \partial_x(\phi \partial_x u + \phi \partial_x v) + \phi \tilde{A}(\phi) \partial_x \phi - \frac{\phi}{1-\phi} \dot{u}. \quad (5b)$$

There are two dimensionless parameters in Eqs. (5), measuring the strength of differential activity, $\tilde{A} = A/\lambda$, and diffusivity, $\tilde{D} = D\Gamma_0/\lambda$.

To understand the stability of a homogenous base state given by $u = u_0$, $\dot{u} = 0$, and $\phi = \phi_0$, we perturb the volume fraction of the phases and the displacement and expand the perturbation in terms of Fourier modes of the form $\propto e^{\omega t + i q x}$ and linearize the equations above. Calculating the largest growing mode to linear order in diffusivity \tilde{D} and to the fourth order in the wave number q gives

$$\Re(\omega_+) \simeq \frac{q^2}{B} \left[-1 + \tilde{A} \phi_0 \left(1 - \frac{\tilde{D} B}{\tilde{A} \phi_0 - 1} \right) \right] - \frac{q^4}{B^2} (\tilde{A} \phi_0 - 1), \quad (6)$$

for $\phi_0 \in [0, 1]$ and $\tilde{A} \phi_0 > 1$, and where $B = 1/(1-\phi_0)$. We see that there is a long wavelength instability with $\Re[\omega_+(q)] > 0$ leading to growth of the homogeneous state on length scales $\gtrsim \ell/\sqrt{B}$ (see Supplemental Material [39], Sec. II). The instability is driven by differential activity A , which competes with frictional momentum transfer between the phases, and diffusion of displacement, velocity, and volume fraction. At the onset of the instability where spatial inhomogeneities in strain are negligible, long wavelength perturbations in volume fraction are amplified because differential activity causes a solid drift velocity \dot{u}

that points toward the maximum of a local inhomogeneity of volume fraction [Fig. 1(c)]. This drift scales as $\dot{u} \propto \tilde{A} \partial_x \phi$ to lowest order in q [Eq. (5b)]. If $A > 0$, the velocity is parallel to the gradient in the solid fraction and thus leads a local increase in the solid volume fraction, while it is zero at the local maximum of the inhomogeneity ($\partial_x \phi = 0$). This velocity profile, together with the volume fraction dependent differential activity $A(\phi)$ [Eq. (3c)], may cause the emergence of spikes in the volume fraction around the initial inhomogeneity where $\partial_x \phi$ is largest. These spikes can move inward due to diffusion and amplify the initial perturbation (see videos in Supplemental Material [39], Sec. VI).

When the diffusivity vanishes, i.e., $\tilde{D} = 0$, the instability occurs for $\tilde{A} > \tilde{A}_c$ with $\tilde{A}_c = 1/\phi_0$ denoting the critical activity (in real units, $A_c = \lambda/\phi_0$). It is asymmetric with respect to volume fraction and the instability vanishes for $\phi_0 \rightarrow 0$ [Fig. 1(a)]. The origin of this asymmetry arises from the difference in passive properties of the two phases [Eqs. (4)]. Symmetry in volume fraction can, for example, be restored if both phases are treated as fluids or as viscoelastic material with equal transport coefficients. The growth rate of the largest growing mode $\omega_+(q)$ is real for all wave numbers if $\tilde{D} = 0$, which indicates a nonoscillatory growth of modes [see Supplemental Material [39], Sec. IV, for plots of $\omega_k(q)$].

For nonzero diffusivity, the critical activity increases [Eq. (6) and Fig. 2(c) black line]. The term $B = 1/(1-\phi_0)$ connected to viscous transport causes the instability to vanish also at large volume fraction [Fig. 1(b)]. In addition, for $\tilde{D} \neq 0$, the growth rate $\omega_k(q)$ can have a nonzero imaginary part. At the transition boundary between the stable and unstable regions, the growth rate is complex for all wave numbers [dark blue (dark gray) in Fig. 1(b)]. However, deep in the unstable regime, the growth rate becomes real for small q , but there remains a complex and unstable band of wave numbers [light blue (light gray) in Fig. 1(b)]. The width of these bands of wave numbers decreases to zero as the diffusivity approaches zero (see Supplemental Material [39], Sec. IV).

These two different characteristics in the growth rate obtained from the linear stability analysis indicate that nonlinear evolution of the patterns might also differ in these regimes. To investigate the pattern dynamics, we numerically solved the nonlinear equations in one and two dimensions; see Supplemental Material [39], Secs. III, V, and VI, for definitions of the used activity functions, details on the numerics, and videos. In one dimension and the limit of zero diffusion, we find that the volume fraction and displacement steadily grow—a behavior that is consistent with a real dispersion relation. In the regime of a purely complex dispersion relation, domains of high and low volume fraction exhibit a tendency to synchronously oscillate with a frequency that is roughly determined by the time to diffuse the size of a domain. On longer

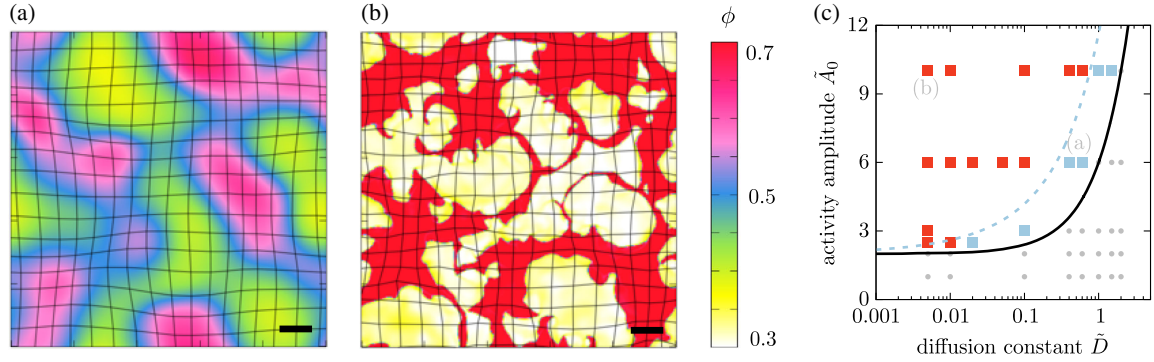


FIG. 2. Patterns and phase diagram in two dimensions obtained from numerically solving Eqs. (3) (see Supplemental Material [39], Secs. V and VI, for details). (a),(b) Two representative snapshots of patterns observed in our active poroelastic model. Black bar depicts the unit length $\ell = \sqrt{\zeta/\Gamma_0}$. Parameters $\phi_0 = 0.5$, and (a) $\tilde{D} = 0.4$, $\tilde{A}_0 = 6$, (b) $\tilde{D} = 0.005$, $\tilde{A}_0 = 10$. The black lines depict the displacements of the solid phase. For lower diffusivity, as expected, we see sharper boundaries as activity-driven demixing progresses. (c) Phase diagram as a function of nondimensional diffusivity \tilde{D} and activity amplitude \tilde{A}_0 . Squares indicate parameters where the numerical solution shows the emergence of spatial-temporal patterns. Blue and red squares correspond to pattern morphologies shown in (a) and (b). The black lines depict the result from the linear stability analysis for Poisson ratio $\nu \approx 0.5$. Parameters above the black curve are linearly unstable; the phase space between the black and blue dashed lines correspond to oscillatory modes for all unstable wave numbers. In the numerics, we considered a specific choice of the activity function (Supplemental Material [39], Sec. III) to confine the range of volume fraction ϕ (color bar). This choice ensures the approximate validity of linear elasticity.

timescales, this oscillating state can spontaneously break the left-right symmetry and the domains collectively move in one direction, reminiscent of traveling fronts found in fluid-fluid biphasic matter in the presence of osmotic forces [49]. In contrast, in the mixed case, where the dispersion relation is real and complex, the domains of high and low volume fraction separated by sharp interfaces seem to drift while they undergo fusion and breakup events.

In two dimensions, we observe similar dynamics. For parameters closer to the transition line, where all unstable modes are oscillatory, the system shows a pulsatory type of pattern [Fig. 2(a)]. Deep in the unstable regime of the stability diagram (e.g., low \tilde{D} and high activity amplitude \tilde{A}_0), domains with sharp and roughened interfaces drift, split, and fuse [Fig. 2(b)]. The onset of the instability and the two pattern morphologies determined numerically match the results obtained via linear stability [Fig. 2(c)]. However, in two dimensions, we do not observe a collectively moving state. The interphase diffusion destabilizes segregated domains on long timescales leading to oscillatory patterns. In systems with low diffusivities, the spatial standard deviation of displacement and volume fraction steadily increases and saturates once the system reaches its quasistationary state, while the velocity becomes vanishingly small.

Our Letter shows how differential activity between the solid and fluid phases that constitute an initially homogeneous poroelastic medium can drive a mechanical instability. It thus complements instabilities driven by differential size [50], differential shape [51], differential diffusion [52], and differential adhesion [53–55]. More specifically, it generalizes one-component active fluid approaches (e.g., [12]) to two phases that can segregate due to the presence of active stress [32,33]. Activity and the interactions between

the phases can cause an instability leading to patches where solid or fluid matter is enriched. Though we have illustrated the instability for a specific set of constitutive equations [Eqs. (4)], the existence of the instability is generic; i.e., it can occur for any combination of passive mechanical properties of the phases. Furthermore, it predicts that, depending on the rate and ability of transport of material and stress in the biphasic material, there will be pulsatile instabilities leading to the assembly, disassembly, and drift of solidlike clusters that undergo fusion and fission. These might play an essential role in cell sorting in tissues, disintegration, and macroscopic contractions in superprecipitated systems [9,10,19] and patterns in the cellular cortex or the cytoplasm [27,28]. We close with the hope that concrete experimental realizations with definite forms of differential activity and material rheology can test the ideas put forward here.

We would like to thank Jakob Löber and Amala Mahadevan for stimulating discussions and Yohai Bar Sinai, David Fronk, and Nicholas Derr for insightful comments and feedback on the manuscript. C. A. W. thanks the German Research Foundation (DFG) for financial support. This research was supported in part by the National Science Foundation under Grant No. NSF PHY-1125915. C. H. R. was supported by the Applied Mathematics Program of the U.S. Department of Energy (DOE) Office of Advanced Scientific Computing Research under Award No. DE-AC02-05CH11231. L. M. was partially supported by the MacArthur Foundation and the Radcliffe Institute Fellowships. L. M. acknowledges partial financial support from NSF DMR 14-20570 and NSF DMR 15-33985.

*Corresponding author.

lmahadev@g.harvard.edu

- [1] V. Schaller, C. Weber, C. Semmrich, E. Frey, and A. R. Bausch, *Nature (London)* **467**, 73 (2010).
- [2] C. Dombrowski, L. Cisneros, S. Chatkaew, R. E. Goldstein, and J. O. Kessler, *Phys. Rev. Lett.* **93**, 098103 (2004).
- [3] H. P. Zhang, A. Be'er, E.-L. Florin, and H. L. Swinney, *Proc. Natl. Acad. Sci. U.S.A.* **107**, 13626 (2010).
- [4] C. A. Weber, T. Hanke, J. Deseigne, S. Léonard, O. Dauchot, E. Frey, and H. Chaté, *Phys. Rev. Lett.* **110**, 208001 (2013).
- [5] F. Backouche, L. Haviv, D. Groswasser, and A. Bernheim-Groswasser, *Phys. Biol.* **3**, 264 (2006).
- [6] A. Kudrolli, G. Lumay, D. Volfson, and L. S. Tsimring, *Phys. Rev. Lett.* **100**, 058001 (2008).
- [7] Y. Sumino, K. H. Nagai, Y. Shitaka, D. Tanaka, K. Yoshikawa, H. Chaté, and K. Oiwa, *Nature (London)* **483**, 448 (2012).
- [8] V. Schaller, C. A. Weber, B. Hammerich, E. Frey, and A. R. Bausch, *Proc. Natl. Acad. Sci. U.S.A.* **108**, 19183 (2011).
- [9] M. Mori, N. Monnier, N. Daigle, M. Bathe, J. Ellenberg, and P. Lénárt, *Curr. Biol.* **21**, 606 (2011).
- [10] P. J. Foster, S. Fürthauer, M. J. Shelley, and D. J. Needleman, *eLife* **4**, e10837 (2015).
- [11] M. Rauzi, P.-F. Lenne, and T. Lecuit, *Nature (London)* **468**, 1110 (2010).
- [12] J. S. Bois, F. Jülicher, and S. W. Grill, *Phys. Rev. Lett.* **106**, 028103 (2011).
- [13] J. Toner, *Phys. Rev. E* **86**, 031918 (2012).
- [14] J. Prost, F. Jülicher, and J. Joanny, *Nat. Phys.* **11**, 111 (2015).
- [15] I. S. Aranson and L. S. Tsimring, *Phys. Rev. E* **71**, 050901 (2005).
- [16] E. Bertin, M. Droz, and G. Grégoire, *J. Phys. A* **42**, 445001 (2009).
- [17] C. A. Weber, F. Thüroff, and E. Frey, *New J. Phys.* **15**, 045014 (2013).
- [18] F. Thüroff, C. A. Weber, and E. Frey, *Phys. Rev. Lett.* **111**, 190601 (2013).
- [19] P. M. Bendix, G. H. Koenderink, D. Cuvelier, Z. Dogic, B. N. Koeleman, W. M. Briehar, C. M. Field, L. Mahadevan, and D. A. Weitz, *Biophys. J.* **94**, 3126 (2008).
- [20] M. Barna and L. Niswander, *Dev. Cell* **12**, 931 (2007).
- [21] J. M. Tabler, C. P. Rice, K. J. Liu, and J. B. Wallingford, *Dev. Biol.* **417**, 4 (2016).
- [22] A. C. Martin *et al.*, *J. Cell Biol.* **188**, 735 (2010).
- [23] E. Hannezo, B. Dong, P. Recho, J.-F. Joanny, and S. Hayashi, *Proc. Natl. Acad. Sci. U.S.A.* **112**, 8620 (2015).
- [24] R. J. Hawkins, R. Poincloux, O. Bénichou, M. Piel, P. Chavrier, and R. Voituriez, *Biophys. J.* **101**, 1041 (2011).
- [25] A. Callan-Jones and R. Voituriez, *New J. Phys.* **15**, 025022 (2013).
- [26] N. Ganai, S. Sengupta, and G. I. Menon, *Nucleic Acids Res.* **42**, 4145 (2014).
- [27] J. Stenhammar, R. Wittkowski, D. Marenduzzo, and M. E. Cates, *Phys. Rev. Lett.* **114**, 018301 (2015).
- [28] S. N. Weber, C. A. Weber, and E. Frey, *Phys. Rev. Lett.* **116**, 058301 (2016).
- [29] A. Grosberg and J.-F. Joanny, *Phys. Rev. E* **92**, 032118 (2015).
- [30] E. Moeendarbary, L. Valon, M. Fritzsche, A. R. Harris, D. A. Moulding, A. J. Thrasher, E. Stride, L. Mahadevan, and G. T. Charras, *Nat. Mater.* **12**, 253 (2013).
- [31] S. Banerjee and M. C. Marchetti, *Soft Matter* **7**, 463 (2011).
- [32] M. Radszuweit, S. Alonso, H. Engel, and M. Bär, *Phys. Rev. Lett.* **110**, 138102 (2013).
- [33] M. Radszuweit, H. Engel, and M. Bär, *PLoS One* **9**, e99220 (2014).
- [34] D. A. Drew, *Annu. Rev. Fluid Mech.* **15**, 261 (1983).
- [35] J. P. Keener, S. Sircar, and A. L. Fogelson, *SIAM J. Appl. Math.* **71**, 854 (2011).
- [36] M. Doi, *J. Phys. Soc. Jpn.* **78**, 052001 (2009).
- [37] H. Tanaka, *Phys. Rev. Lett.* **71**, 3158 (1993).
- [38] H. Tanaka, *J. Phys. Condens. Matter* **12**, R207 (2000).
- [39] See Supplemental Material at <http://link.aps.org/supplemental/10.1103/PhysRevLett.120.248003> for videos and more information, which includes Refs. [10,40–43].
- [40] Specifically, the influence on the numerical integration of the added inertia terms are negligible if $\hat{\rho} = \rho v_0^2 / \lambda \ll 1$.
- [41] A. J. Chorin, *Math. Comput.* **22**, 745 (1968).
- [42] G. R. Dennis, J. J. Hope, and M. T. Johnsson, *Comput. Phys. Commun.* **184**, 201 (2013).
- [43] COMSOL MULTIPHYSICS® ver. 5.0., COMSOL AB, Stockholm, Sweden, www.comsol.com.
- [44] S. Barry and M. Holmes, *IMA J. Appl. Math.* **66**, 175 (2001).
- [45] S. C. Cowin and L. Cardoso, *Mech. Mater.* **44**, 47 (2012).
- [46] J. Skotheim and L. Mahadevan, *Proc. R. Soc. A* **460**, 1995 (2004).
- [47] The osmotic pressure can also be absorbed into a renormalized activity, which only shifts the transition to larger activities.
- [48] M. Spiegelman and D. McKenzie, *Earth Planet. Sci. Lett.* **83**, 137 (1987).
- [49] N. Cogan, M. Donahue, and M. Whidden, *Phys. Rev. E* **86**, 056204 (2012).
- [50] S. Asakura and F. Oosawa, *J. Chem. Phys.* **22**, 1255 (1954).
- [51] L. Onsager, *Ann. N.Y. Acad. Sci.* **51**, 627 (1949).
- [52] A. M. Turing, *Phil. Trans. R. Soc. B* **237**, 37 (1952).
- [53] P. J. Flory, *J. Chem. Phys.* **10**, 51 (1942).
- [54] M. L. Huggins, *J. Phys. Chem.* **46**, 151 (1942).
- [55] M. S. Steinberg, *J. Exp. Zool.* **173**, 395 (1970).

Supplemental Material:
Differential-activity driven instabilities in biphasic active matter

Christoph A. Weber,¹ Chris H. Rycroft,^{1,2} and L. Mahadevan³

¹*Paulson School of Engineering and Applied Sciences,
Harvard University, Cambridge, MA 02138, USA*

²*Mathematics Group, Lawrence Berkeley National Laboratory, Berkeley, CA 94720, USA*

³*Paulson School of Engineering and Applied Sciences,
Department of Physics, Department of Organismic and Evolutionary Biology,
Harvard University, Cambridge, MA 02138, USA*

CONTENTS

I. Origin of diffusion in biphasic matter	2
II. Critical wavenumber	2
III. Properties and possible choices of differential activity	3
A. Properties of differential activity	3
B. Possible choices of differential activity	3
IV. Growth rates as a function of wavenumber for different parameters	4
V. Details of numerical implementation	4
A. Dynamical equations considered in the numerical studies	4
B. Numerical methods used to solve dynamical equations in two dimensions	6
C. Numerical solution of dynamical equations in one dimension	7
VI. Movie descriptions	7
References	7

I. ORIGIN OF DIFFUSION IN BIPHASIC MATTER

In our model for biphasic active matter we introduced a relative diffusive flux $j_\alpha^{(1)} = -j_\alpha^{(2)} =: j_\alpha$ in the transport equations of volume fraction, $\partial_t \phi^{(i)} = -\partial_\alpha \left(\phi^{(i)} v_\alpha^{(i)} + j_\alpha^{(i)} \right)$, though the velocity $v_\alpha^{(i)}$ already captures the movement of each phase. Below we will discuss one possible mechanism for how such a diffusive flux can emerge and that it can be written as $j_\alpha = -D \partial_\alpha \phi$, where D denotes the diffusion constant.

This relative flux can for example stem from unbinding events of components that belong to one of the phases. Here, a bound state refers to filaments connected to other filaments by crosslinks and/or molecular motors, or active cells in a tissues connected by integrins for example. Unbinding here means that the constituents loose their connections to neighboring filaments or cells and can thus diffuse more or less freely. We introduce ϕ as the volume fraction of the bound solid-like components (filaments, cells, ...) and ϕ_{off} as the subpopulation of the corresponding unbound components diffusing with a diffusion constant D_{off} . We consider that bound plus unbound components are conserved. For simplicity, we assume a local relationship between these components that can be written as $\phi_{\text{off}}(\phi) = \mathcal{G}(\phi)$. Moreover, unbinding occurs with a rate γ_2 , while binding happens with a rate γ_1 . The corresponding equations are:

$$\partial_t \phi_{\text{off}} = D_{\text{off}} \nabla^2 \phi_{\text{off}} - \gamma_1 \phi_{\text{off}} + \gamma_2 \phi, \quad (\text{S1})$$

$$\partial_t \phi = \nabla \cdot (\phi \mathbf{v}^{(1)}) + \gamma_1 \phi_{\text{off}} - \gamma_2 \phi. \quad (\text{S2})$$

Assuming a fast binding dynamics, $\partial_t \phi_{\text{off}} \simeq 0$,

$$\partial_t \phi \simeq \nabla \cdot (\phi \mathbf{v}^{(1)}) + D_{\text{off}} \nabla \cdot (\mathcal{G}(\phi)' \nabla \phi). \quad (\text{S3})$$

Say $\mathcal{G}(\phi) \simeq \mathcal{G}_0 + \mathcal{G}_1 \phi$, the flux \mathbf{j} in $\partial_t \phi = -\nabla \cdot \mathbf{j}$, has the form of Fick's law: $\mathbf{j} = -D \nabla \phi$ with a constant diffusion coefficient $D = D_{\text{off}} \mathcal{G}_1$.

II. CRITICAL WAVENUMBER

Eq. (6) in the main text can be used to estimate the critical wavenumber below which the long wave length instability occurs. $\Re(\omega_+) = 0$ yields $q = 0$ (due to the conservation of the fraction of each phase), and

$$q_{\text{max}} \simeq \sqrt{B \left(1 - \tilde{D} \frac{B \tilde{A} \phi_0}{(\tilde{A} \phi_0 - 1)^2} \right)}. \quad (\text{S4})$$

The instability occurs for $\Re(\omega_+) > 0$ and $q < q_{\max}$. Note that Eq. (S4) is only valid for small diffusivities, $\tilde{D} \ll 1$, as $\Re(\omega_+)$ given in Eq. (6) (main text) stems from a Taylor expansion for small diffusivities \tilde{D} . Thus, there is no actual sign change of q_{\max} as \tilde{D} is increased. However, increasing the diffusivity shifts the occurrence of the instability to larger length scales. This trend is reasonable as diffusion flattens volume fraction inhomogeneities. For negligible diffusivity, an initially homogenous state must be perturbed with a wavenumber $q < q_{\max} \simeq \sqrt{B}$ which corresponds to a length scale larger than $1/\sqrt{B}$. In real units this critical length scale reads

$$\frac{\ell}{\sqrt{B}}, \quad (\text{S5})$$

where $\ell = \sqrt{\zeta/\Gamma_0}$ with ζ and Γ_0 as the solid viscosity and the friction between the phases. Thus, the length used to rescale our dynamic equations, ℓ , is the fundamental length scale for the occurrence of the long wave length instability.

III. PROPERTIES AND POSSIBLE CHOICES OF DIFFERENTIAL ACTIVITY

A. Properties of differential activity

Differential activity is the driver for the instability discussed in our letter. In this section we discuss some basic properties of the differential activity function,

$$A(\phi) = \left[\frac{A^{(1)}}{\phi} + \frac{A^{(2)}}{1-\phi} + \frac{d}{d\phi} (A^{(1)} - A^{(2)}) \right]. \quad (\text{S6})$$

Equation (S6) implies that differential activity does not vanish for equal activities, $A^{(1)} = A^{(2)}$. However, differential activity can vanish even for non-zero activity in each phase, $A^{(i)} \neq 0$. One possibility is that activities cancel within the same phase, i.e. $A^{(1)} = A_{0,1}/\phi$ and $A^{(2)} = A_{0,2}/(1-\phi)$, where $A_{0,i}$ is some constant. The other possibility is that the activity of one phase cancels the activity of the other phase, i.e. $A^{(1)} = \mp A_0\phi$ and $A^{(2)} = \pm A_0(1-\phi)$, with A_0 denoting some constant.

In the main text we discuss the case of constant differential activity. The differential activity A can be constant and non-zero for $A^{(1)} = \pm A_{0,1}\phi$ and $A^{(2)} = \pm A_{0,2}(1-\phi)$, or $A^{(1)} = A^{(2)} = A_0\phi(1-\phi)$.

B. Possible choices of differential activity

The shape and dependencies of the activities depend on the particular system of interest. Next to a constant differential activity one could consider an asymmetric case where phase 2 is passive ($A^{(2)} = 0$) and phase 1 is active with $A^{(1)} = A_0\phi(1-\phi)$, leading to a differential activity $A = A_0(2-3\phi)$ (Eq. (S6)). Here, A_0 characterizes the amplitude of the activity. In this case the generation of active stress vanishes in the absence of phase 1 or 2, respectively. This asymmetric case is qualitatively motivated by super-precipitated systems and tissues [1–7], where one phase is passive (intestinal fluid) while the other phase is active (filaments, cells). Moreover, activity requires a non-zero fraction of active components ($A^{(1)} \propto \phi$) while there could exit an inhibitory mechanism as the active components get crowded ($A^{(1)} \propto -\phi^2$). For such an activity function linear stability suggests that an instability occurs if the activity amplitude A_0 is larger than the critical activity $\tilde{A}_{0,c} = (\phi_0(2-3\phi_0))^{-1}$ (for vanishing diffusivity $\tilde{D} = 0$). Interestingly, the instability can occur for both, positive (expansions) and negative (contractions) activity amplitudes \tilde{A}_0 (Fig. (S1)). We tested this choice of activities in our one-dimensional numerical studies and found that the emergence of spatial-temporal patterns is consistent with the results from the linear stability analysis. However, for parameters deeply in the unstable region of the stability diagram, large local strain, $\partial_x u$, can build up during the pattern formation violating the small strain limit of the used Hooke's law. Thus we considered an activity function which ensures that domains cannot exhibit porosities below ϕ_{\min} or above ϕ_{\max} . This also restricts the system to small or moderate strains. The activities thus read

$$A^{(1)} = A_0 \left[(\phi - \phi_0) - a(\phi - \phi_0)^3 \right], \quad (\text{S7})$$

$$A^{(2)} = 0, \quad (\text{S8})$$

where A_0 denotes the activity amplitude (non-dimensional activity amplitude $\tilde{A}_0 = A_0/\lambda$). It sets the scale of the active stress, but not the fixed points where the activity $A^{(1)}$ vanishes to zero. The latter is determined by the parameter $a > 0$. Its value restricts the dynamics within the volume fractions $\phi_{\min} = \phi_0 - 1/\sqrt{a}$ and $\phi_{\max} = \phi_0 + 1/\sqrt{a}$. In our letter we fix the mean volume fraction to $\phi_0 = 0.5$ and $a = 20$, leading to $\phi_{\min} \approx 0.276$ and $\phi_{\max} \approx 0.724$.

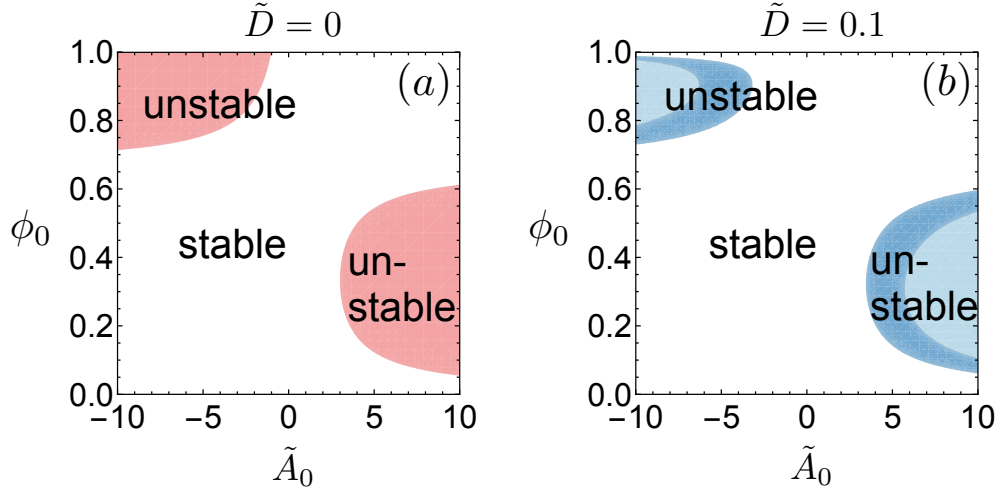


FIG. S1. Stability diagrams indicating the parameter regimes where the homogeneous base state is stable or unstable for the case of an asymmetric choice of activity, $A^{(2)} = 0$ and $A^{(1)} = A_0\phi_0(1 - \phi_0)$ with $\tilde{A}_0 = A_0/\lambda$, and (a) $\tilde{D} = 0$ and (b) $\tilde{D} = 0.1$. The colored regions depict $\Re(\omega_+) > 0$. Dark and light blue correspond to $\Im(\omega_k) \neq 0$ for all q , or for a finite waveband, respectively.

IV. GROWTH RATES AS A FUNCTION OF WAVENUMBER FOR DIFFERENT PARAMETERS

V. DETAILS OF NUMERICAL IMPLEMENTATION

A. Dynamical equations considered in the numerical studies

For our numerical studies we consider a biphasic mixture of a fluid (f) and solid-like (s) phase. Each phase (i) is described by the hydrodynamic variables: velocity $v_\alpha^{(i)}$, volume fraction $\phi^{(i)}$ and displacement $u_\alpha^{(i)}$ with $\partial_t u_\alpha^{(i)} = v_\alpha^{(i)}$. For the numerical integration of the dynamical equations we introduce an inertia term on the left hand side of Eqs. (2a) and (2b) (main text) to make the numerical implementation straightforward (time evolution is easier than the force balance constraint). However, the quantitative influence on the solutions is expected to be negligible if the mass density ρ is small enough [8]. The full non-linear equations for the active biphasic system considered in the numerical studies read

$$\partial_t \phi = -\partial_\alpha (\phi v_\alpha^s) + D \partial_\alpha^2 \phi, \quad (\text{S9a})$$

$$0 = \partial_\alpha [\phi v_\alpha^s + (1 - \phi) v_\alpha^f], \quad (\text{S9b})$$

$$\partial_t u_\alpha = v_\alpha^s, \quad (\text{S9c})$$

$$\rho \phi \partial_t v_\alpha^s = \partial_\beta (\phi \sigma_{\alpha\beta}^s) - \phi \partial_\alpha p + \Gamma_0 \phi (1 - \phi) (v_\alpha^f - v_\alpha^s), \quad (\text{S9d})$$

$$\rho (1 - \phi) \partial_t v_\alpha^f = \partial_\beta ((1 - \phi) \sigma_{\alpha\beta}^f) - (1 - \phi) \partial_\alpha p - \Gamma_0 \phi (1 - \phi) (v_\alpha^f - v_\alpha^s), \quad (\text{S9e})$$

where p denotes the pressure ensuring the incompressibility condition Eq. (S9b). The stress tensors of the solid (s) and fluid (f) phases are

$$\sigma_{\alpha\beta}^s = \lambda \delta_{\alpha\beta} \partial_\gamma u_\gamma + G (\partial_\alpha u_\beta + \partial_\beta u_\alpha) \quad (\text{S10})$$

$$\begin{aligned} & + \bar{\lambda} \delta_{\alpha\beta} \partial_\gamma v_\gamma^s + \eta (\partial_\alpha v_\beta^s + \partial_\beta v_\alpha^s) + A_0 [(\phi - \phi_0) - a(\phi - \phi_0)^3] \delta_{\alpha\beta}, \\ & \sigma_{\alpha\beta}^f = 0, \end{aligned} \quad (\text{S11})$$

where λ is the first Lamé parameter and $G = \lambda(1 - 2\nu)/(2\nu)$ is the shear modulus, and ν denotes the Poisson ratio. Moreover, $\bar{\lambda}$ is the bulk viscosity and η is the shear viscosity. The second viscosity $\zeta = \bar{\lambda} + 2\eta/3$. We used the choice of the activity function given in Eq. (S7). For the fluid phase we neglected contributions proportional to velocity gradients because they are expected to be small on scales above the size of the solid pores. In addition, the solid viscosities typically exceeds the fluid viscosities by several orders of magnitude.

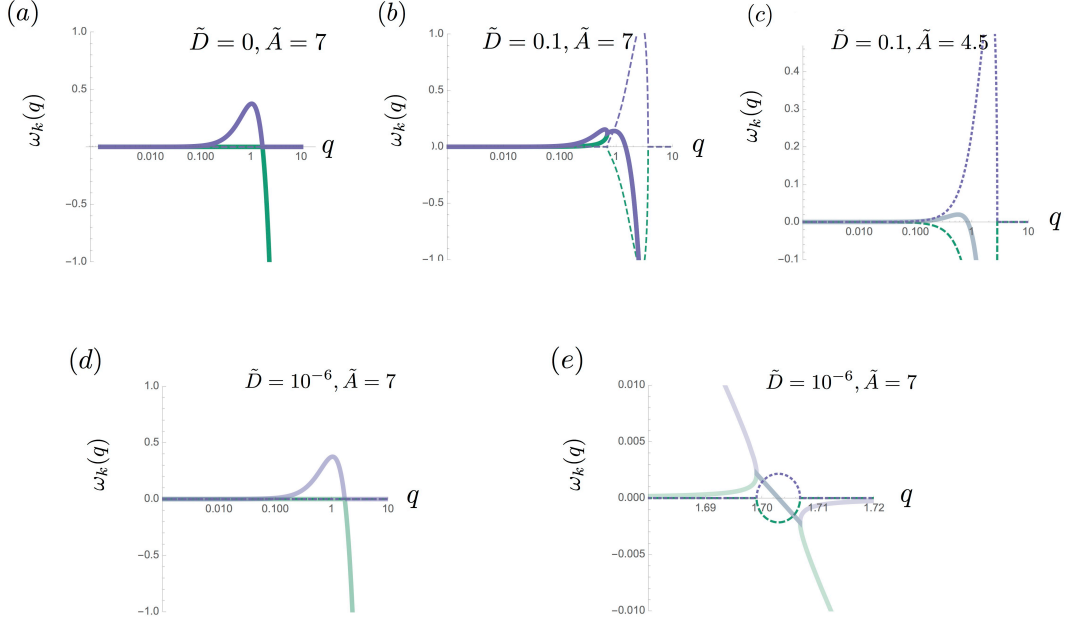


FIG. S2. Growth rate $\omega_k(q)$ as a function of wavenumber for different parameters for our model one-dimensional model discussed in the main text. Solid lines indicate the real part of the growth rate, $\Re[\omega_k(q)]$, while the dashed lines correspond to the imaginary part, $\Im[\omega_k(q)]$. Parameters are $\phi_0 = 0.35$ and the remaining parameters are shown on each plot. (a) For $\tilde{D} = 0$, the growth rate of the largest growing mode, $\omega_+(q)$ (purple), is real for all wavenumbers indicating a non-oscillatory growth of modes. (b) As the diffusivity \tilde{D} increases, the growth rate becomes real for large q but there remains a complex growth rate for a finite waveband at larger wavenumbers (light blue region in the phase diagram, main text, Fig. 2b). (c) Close to the transition where the instability vanishes (here we have decreased \tilde{A} relative to (b)), the growth rate is complex for all wavenumbers (dark blue region in the phase diagram, main text, Fig. 2b). (d) However, deeply in the region of the phase diagram where the instability occurs, the width of the complex waveband (as shown in (b)) decreases to zero as the diffusivity approaches zero. (e) This behavior is nicely visible in the wavenumber zoom-in corresponding to (d).

We rescale length and time as $x \rightarrow \ell \cdot x$ with $\ell = \sqrt{\lambda/\Gamma_0}$, and $t \rightarrow (\ell/v_0) \cdot t$, and consider a velocity rescaling $v_\alpha^{(i)} \rightarrow v_\alpha^{(i)} \cdot v_0$. The dimensional pressure and stress are $p \rightarrow p \cdot \lambda$ and $\sigma_{\alpha\beta}^{(i)} \rightarrow \sigma_{\alpha\beta}^{(i)} \cdot \lambda$. After this rescaling there are five dimensionless parameters in more than one dimension, namely $\tilde{A}_0 = A_0/\lambda$, $\tilde{D} = D/(\ell v_0)$, $\tilde{G} = G/\lambda$, $V = v_0 \bar{\lambda}/(\lambda \ell) = v_0 \sqrt{\Gamma_0 \bar{\lambda}}/\lambda$, and $\tilde{\eta} = V \eta/\bar{\lambda}$. In one dimension the two shear parameters $(\tilde{G}, \tilde{\eta})$ do not exist leading to three parameters. In the main text we considered the special case where the velocity scale $V = 1$ leaving us with two non-dimensional parameters, namely the activity amplitude \tilde{A}_0 and the diffusivity \tilde{D} .

The dimensionless equations used for numerical discretization are

$$\partial_t \phi = -\partial_\alpha (\phi v_\alpha^s) + \tilde{D} \partial_\alpha^2 \phi, \quad (\text{S12a})$$

$$0 = \partial_\alpha [\phi v_\alpha^s + (1 - \phi) v_\alpha^f], \quad (\text{S12b})$$

$$\partial_t u_\alpha = v_\alpha^s, \quad (\text{S12c})$$

$$\hat{\rho} \phi \partial_t v_\alpha^s = \partial_\beta (\phi \sigma_{\alpha\beta}^s) - \phi \partial_\alpha p + V \phi (1 - \phi) (v_\alpha^f - v_\alpha^s), \quad (\text{S12d})$$

$$\hat{\rho} (1 - \phi) \partial_t v_\alpha^f = -(1 - \phi) \partial_\alpha p - V \phi (1 - \phi) (v_\alpha^f - v_\alpha^s), \quad (\text{S12e})$$

where the dimensionless mass density is $\hat{\rho} = \rho v_0^2/\lambda$.

ϕ_0	\tilde{D}	\tilde{A}_0	ν	V	$\tilde{\eta}$	$\hat{\rho}$	a
0.5	0.005–5	0–10	0.48 ($\tilde{G} \approx 0.0417$)	0.06	0.02	0.02	20

TABLE S1. A list of fixed parameters used to numerically solve Eq. (S16) in two spatial dimensions with the solid stress tensor given in Eq. (S10). For the numerical results please refer to main text, Fig. 3 and movies Sec. VI.

B. Numerical methods used to solve dynamical equations in two dimensions

In the numerical integration we consider periodic boundary conditions. The two-dimensional simulations are performed with a custom C++ code and use an $N \times N$ grid for non-dimensional system size $(L/\ell) \times (L/\ell)$, where $\ell = \sqrt{\lambda/\Gamma_0}$ is the unit length and L is the system size. The spatial derivatives are discretized using second-order finite-differences. The time derivatives are discretized by an Euler scheme with a time increment of Δt and a discrete time $t = n \cdot \Delta t$, where n denotes the n -th time step.

In two dimensions, the essential step in the numerical integration is the calculation of the pressure in a way that the incompressibility holds (Eq. (S12b)). To this end, we apply a variant of Chorin's projection method as used in the integration of the incompressible Navier–Stokes equations [9]. This method amounts to splitting the integration of Eqs. (S12d) and (S12e) into three parts. The first part calculates intermediate velocities $v_\alpha^{s,*}$ and $v_\alpha^{f,*}$ by neglecting the pressure gradient and relaxing the incompressibility constraint. These velocities are then used in the second part to compute the pressure via solving a Poisson problem. In the final part, the pressure is employed to project the velocities to satisfy the incompressibility constraint.

The first part of the projection step can thus be written as

$$\hat{\rho} \frac{v_\alpha^{s,*} - v_\alpha^s(n)}{\Delta t} = \phi(n)^{-1} \partial_\beta (\phi(n) \sigma_{\alpha\beta}^s(n)) + V (1 - \phi(n)) (v_\alpha^f(n) - v_\alpha^s(n)) , \quad (\text{S13a})$$

$$\hat{\rho} \frac{v_\alpha^{f,*} - v_\alpha^f(n)}{\Delta t} = -V \phi(n) (v_\alpha^f(n) - v_\alpha^s(n)) . \quad (\text{S13b})$$

The second step can be derived by writing down the third step of the projection method,

$$\hat{\rho} \frac{v_\alpha^s(n+1) - v_\alpha^{s,*}}{\Delta t} = -\partial_\alpha p(n+1) , \quad (\text{S14a})$$

$$\hat{\rho} \frac{v_\alpha^f(n+1) - v_\alpha^{f,*}}{\Delta t} = -\partial_\alpha p(n+1) . \quad (\text{S14b})$$

The third step requires the knowledge of the pressure $p(n+1)$ at time step $n+1$ and computes the incompressible velocities $v_\alpha^s(n+1)$ and $v_\alpha^f(n+1)$ at time step $n+1$. The pressure is computed in the second step. Since $v_\alpha^s(n+1)$ and $v_\alpha^f(n+1)$ obey the incompressibility condition, multiplying Eq. (S14a) by $\phi(n)$ and Eq. (S14b) by $(1 - \phi(n))$, and adding up both equations, applying the divergence and using the incompressibility condition for the incompressible velocities (Eq. (S12b)), we find

$$\partial_\alpha^2 p(n+1) = \frac{\hat{\rho}}{\Delta t} \partial_\alpha [\phi(n) v_\alpha^{s,*} + (1 - \phi(n)) v_\alpha^{f,*}] . \quad (\text{S15})$$

The equation above represents the second step of the projection step. It is an elliptic problem, and is solved using a custom C++ implementation of the geometric multigrid method. Solving this equation gives the pressure $p(n+1)$, which is required in the third steps as described above.

In summary, given the fields $\phi(n)$, $v_\alpha^s(n)$, $v_\alpha^f(n)$ and $u_\alpha(n)$ at time step n , the full projection based algorithm in

time is

$$\hat{\rho} \frac{v_{\alpha}^{s,*} - v_{\alpha}^s(n)}{\Delta t} = \phi(n)^{-1} \partial_{\beta} (\phi(n) \sigma_{\alpha\beta}^s(n)) + V (1 - \phi(n)) (v_{\alpha}^f(n) - v_{\alpha}^s(n)) , \quad (\text{S16a})$$

$$\hat{\rho} \frac{v_{\alpha}^{f,*} - v_{\alpha}^f(n)}{\Delta t} = -V \phi(n) (v_{\alpha}^f(n) - v_{\alpha}^s(n)) , \quad (\text{S16b})$$

$$\partial_{\alpha}^2 p(n+1) = \frac{\hat{\rho}}{\Delta t} \partial_{\alpha} [\phi(n) v_{\alpha}^{s,*} + (1 - \phi(n)) v_{\alpha}^{f,*}] , \quad (\text{S16c})$$

$$\hat{\rho} \frac{v_{\alpha}^s(n+1) - v_{\alpha}^{s,*}}{\Delta t} = -\partial_{\alpha} p(n+1) , \quad (\text{S16d})$$

$$\hat{\rho} \frac{v_{\alpha}^f(n+1) - v_{\alpha}^{f,*}}{\Delta t} = -\partial_{\alpha} p(n+1) , \quad (\text{S16e})$$

$$\frac{\phi(n+1) - \phi(n)}{\Delta t} = -\partial_{\alpha} (\phi(n) v_{\alpha}^s(n)) + \tilde{D} \partial_{\alpha}^2 \phi(n) , \quad (\text{S16f})$$

$$\frac{u_{\alpha}(n+1) - u_{\alpha}(n)}{\Delta t} = v_{\alpha}^s(n) . \quad (\text{S16g})$$

The spatial derivatives are implemented using a second-order finite difference discretization (not shown). Parameters for the integration in two spatial dimensions are given in Table S1.

C. Numerical solution of dynamical equations in one dimension

In one dimension, the projection steps are not necessary since the incompressibility condition (Eq. (S12b)) implies a linear relationship between the velocities. With appropriate boundary conditions, $v^f = -v^s \phi / (1 - \phi)$. Therefore, the pressure is determined and can be substituted. For the one-dimensional studies we considered a velocity scale $V = 1$ for simplicity, leading to

$$\partial_t \phi = -\partial_x (\phi v) + \tilde{D} \partial_x^2 \phi , \quad (\text{S17a})$$

$$\partial_t u = v , \quad (\text{S17b})$$

$$\hat{\rho} \frac{\phi}{1 - \phi} \partial_t v = \partial_x (\phi \partial_x u) + \partial_x (\phi \partial_x v) + \phi (A/\lambda) \partial_x \phi - \frac{\phi}{1 - \phi} v^s , \quad (\text{S17c})$$

where we abbreviated $v = v^s$ and $A(\phi)$ denotes the differential activity (main text, Eq. (3c)). We verified our one-dimensional results by our implementation as outlined above with the results obtained from a spectral based solver (XMDS2 [10]) and a finite element solver (Comsol Multiphysics[®] software [11]). The movies in 1D were rendered using the Comsol software.

VI. MOVIE DESCRIPTIONS

We have attached two movies for the one-dimensional (1D) equations (S17), and two for the two-dimensional (2D) equations (S16). If not stated below, parameters are given in Table S1.

- (1) 1D: oscillating dynamics and collective motion. $\tilde{D} = 0.4$, $\phi_0 = 0.5$, $\tilde{A}_0 = 6$, duration $T = 500$, $L/\ell = 50$, grid points $N = 500$.
- (2) 1D: drifting domains undergoing fusion and break-up. $\tilde{D} = 0.005$, $\phi_0 = 0.5$, $\tilde{A}_0 = 10$, duration $T = 250$, $L/\ell = 50$, grid points $N = 500$.
- (3) 2D: pulsatory-type of dynamics. $\tilde{D} = 0.4$, $\phi_0 = 0.5$, $\tilde{A}_0 = 6$, duration $T = 100$, $L/\ell = 10$, grid points $N = 256$.
- (4) 2D: drifting domains undergoing fusion and break-up. $\tilde{D} = 0.005$, $\phi_0 = 0.5$, $\tilde{A}_0 = 10$, duration $T = 100$, $L/\ell = 10$, grid points $N = 256$.

- [2] E. Moeendarbary *et al.*, Nature materials **12**, 253 (2013).
- [3] M. Mori *et al.*, Current Biology **21**, 606 (2011).
- [4] P. M. Bendix *et al.*, Biophysical Journal **94**, 3126 (2008).
- [5] P. J. Foster, S. Forthauer, M. J. Shelley, and D. J. Needleman, eLife **4**, e10837 (2015).
- [6] M. Radszuweit, S. Alonso, H. Engel, and M. Bär, Phys. Rev. Lett. **110**, 138102 (2013).
- [7] M. Radszuweit, H. Engel, and M. Bär, PloS one **9**, e99220 (2014).
- [8] Specifically, the influence on the numerical integration of the added inertia terms are negligible if $\hat{\rho} = \rho v_0^2 / \lambda \ll 1$.
- [9] A. J. Chorin, Mathematics of Computation **22**, 745 (1968).
- [10] G. R. Dennis, J. J. Hope, and M. T. Johnsson, Computer Physics Communications **184**, 201 (2013).
- [11] COMSOL Multiphysics[®] v. 5.0. www.comsol.com. COMSOL AB, Stockholm, Sweden.